Broadband X-ray analysis of 1E 1740.7−2942: constraints on spin, inclination and a tentative black hole mass

Paulo E. Stecchini[1]⋆, F. D'Amico[1], F. Jablonski[1], M. Castro[2] and J. Braga[1]

[1]*Instituto Nacional de Pesquisas Espaciais, Av. dos Astronautas 1758, 12227-010, S.J. Campos–SP, Brazil*

[2]*Universidade Estadual de Campinas, Cidade Universitaria Zeferino Vaz, 13083-853, Campinas–SP, Brazil*

ABSTRACT

1E 1740.7−2942 is one of the strongest hard X-ray emitters in the Galactic Centre region, believed to be a black hole in a high-mass X-ray binary system. Although extensively studied in X-rays, many aspects about the underlying nature of the system are still unknown. For example, X-ray data analyses of 1E 1740.7−2942 up to date have not yet unveiled the signature of a reflection component, whose modelling could be used to estimate parameters such as the spin of the black hole and inclination of the disc. We report here on the determination of these parameters from the analysis of the reflection component present in a public *NuSTAR* observation which hasn't been subject to any previous study. We include *XMM-Newton* and *INTEGRAL* data to build a combined spectrum, enabling a joint analysis of both the disc and comptonisation components. Results point to a relatively high inclination disc $\gtrsim 50°$ $(3\,\sigma)$ and a near-maximum speed rotating black hole. The former is in agreement with a previous radio study and the latter is reported here for the first time. Lastly, we follow the methodology of recent efforts to weight black holes with only X-ray spectra and find results that suggest a black hole mass of about $5\,M_\odot$ for 1E 1740.7−2942.

Key words: accretion, accretion discs—X-rays: binaries—black hole physics—stars: individual (1E 1740.7-2942)

1 INTRODUCTION

The source 1E 1740.7−2942 was discovered by the *Einstein Observatory* satellite during the first Galactic Plane X-ray survey (Hertz & Grindlay 1984) and classified as a black hole candidate due to its spectral similarities to Cygnus X-1 (Sunyaev et al. 1991). This classification was later supported by the observation of radio jets coming from the main X-ray source (Mirabel et al. 1992), which also identified 1E 1740.7−2942 as a microquasar. Known to be among the brightest hard X-ray sources around the Galactic Centre (GC), 1E 1740.7−2942 is observed to spend most of the time in the low/hard state (LHS) of emission (see, e.g., Castro et al. 2014) – a state well described by thermal comptonisation models. The permanence in this state had already been verified from studies with data from *RXTE + INTEGRAL* (del Santo et al. 2005), the telescopes on-board *Suzaku* (Reynolds & Miller 2010) and *NuSTAR + INTEGRAL* (Natalucci et al. 2014). These last two works reported no strong evidence of a reflection component in their spectra. There is, until now, no optical or infrared counterpart confirmed for

1E 1740.7−2942 – which is usually attributed to the high galactic extinction towards the GC at these wavelengths (see, e.g., Gallo & Fender 2002). In one of the most recent attempts, Martí et al. (2010) have successfully identified a single near-infrared source towards the system's location. The study suggested two hypotheses to explain the counterpart candidate detected: an Active Galactic Nucleus projected along the line of sight of the system or a black hole high-mass X-ray binary. The former hypothesis was discarded by Luque-Escamilla et al. (2015) after analysing the bi-polar radio jets of 1E 1740.7−2942. A periodic modulation of ∼ 12.6 days, reported by Smith et al. (2002) and Stecchini et al. (2017), if attributed to the orbital period of the system, also supports the proposition of 1E 1740.7−2942 being part of a high-mass X-ray binary system, as this modulation is much longer than most known black hole low-mass X-ray binaries orbital periods (see, e.g., Corral-Santana et al. 2016). Without an observable counterpart the relative motions between the compact object and the companion cannot be determined, preventing the mass function $f(M)$ of the system from being established. Hence, apart from the rough estimate of the distance to the source – assumed to be that to the GC – and the suggestion of a high inclination disc (from

⋆ E-mail: paulo.stecchini@inpe.br

the presence of bi-polar radio jets, Mirabel et al. 1992), many dynamical parameters are still unknown for 1E 1740.7−2942.

In this study we gather public available data of 1E 1740.7−2942 from *XMM-Newton* (Jansen et al. 2001), *NuSTAR* (Harrison et al. 2013) and *INTEGRAL* (Winkler et al. 2003) to build a broadband spectrum, whose total energy coverage (∼ 2–200 keV) allows us to inspect the disc, reflection and comptonisation components altogether. Using the X-ray spectral-fitting program XSPEC (Arnaud 1996) we apply from simple powerlaw models to some of the most popular comptonisation models available and compare our results with values found in the literature for 1E 1740.7−2942. Our main goal, however, is to model the reflection component, which we regard to be present in the *NuSTAR* data. The presence of this component is a necessary condition to apply the so-called X-ray reflection spectroscopy method (or iron line method), which can directly provide parameters such as the spin and inclination of the system. Finally, motivated by the lack of information with respect to the mass of the system and by the recent efforts to weight black holes from X-ray spectra alone (see, e.g., Parker et al. 2016), we analyse the disc spectrum (which, due to *XMM-Newton* data we can model down to 2 keV) with a mass-dependent model to speculate over this parameter.

2 OBSERVATIONS

2.1 *NuSTAR*

1E 1740.7−2942 was observed for calibration purposes by the *NuSTAR* satellite on three occasions, all of which occurred within ∼ 2 months of the mission's launching. Two of the observations (of ∼2 ks and ∼6 ks exposure times) have been analysed by Natalucci et al. (2014), which reported the absence of any strong iron line or reflection components. We focus our analysis on the other observation – the longest available (of ∼ 10 ks) – and which hasn't yet been subject to any study found in the literature. The data from the observation (ObsID 10002012001) were reduced using the standard procedures of the *NuSTAR* Data Analysis Software (NuS-TARDAS) for both FPMA and FPMB cameras. Source and background spectra were extracted from a ∼ 90″ circular region centred on the source position and from a source-free region of ∼ 150″, respectively. Due to a possible overwriting issue during the observation, FPMB camera had ∼ 20% less exposure time than FPMA and therefore was not included in this analysis. The FPMA data were rebinned to have at least 50 counts per spectral bin prior to the analysis conducted with XSPEC.

Figure 1 shows (rebinned for plotting purposes only) the data and the residuals (as data/model) for an absorbed powerlaw model (`phabs*powerlaw` from XSPEC). The best-fitting ($\chi^2\nu = \frac{562}{507} = 1.11$, where χ^2 is the usual chi-square statistics, ν is the number of degrees of freedom and the last value is the reduced χ^2) parameters were N_H ($\times 10^{22}$) = 13.2 ± 1.5 cm^{-2} and a powerlaw index (Γ) of 1.76 ± 0.03. These values differ slightly from those reported for the other two *NuSTAR* observations (i.e., $N_H > 18 \times 10^{22}$ and $\Gamma \lesssim 1.7$); the interstellar absorption found here is in better agreement with previously reported values from other missions (see, e.g., Gallo & Fender 2002, Reynolds & Miller 2010 and Castro et al.
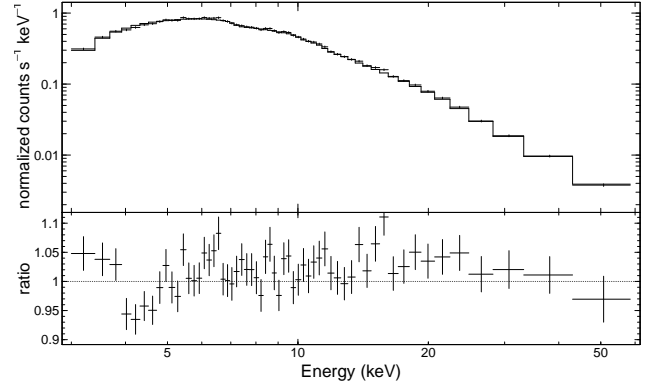

Figure 1. Spectrum of 1E 1740.7−2942 from FPMA and the residuals for an absorbed powerlaw model. Data were rebinned for plotting purposes only.

2014) and the steeper photon index – although within the range of indices that describe well the low/hard state (1.4 ≤ Γ ≤ 2.1, see, e.g., Remillard & McClintock 2006) – may indicate that 1E 1740.7−2942 was going through a state transition or was in a "softer" low/hard state. As also pointed out by Natalucci et al. (2014) for the other two observations, the residuals at lower energies suggest that a soft component is required. In fact, adding a multicolour disc blackbody component (`diskbb`, Mitsuda et al. 1984; Makishima et al. 1986) to the model and applying an F-test gives a very low probability (∼ 10^{-6}) against the null hypothesis. Also noticeable from the residuals in Figure 1 are a slight excess at about 15–30 keV – which could be due to a reflection feature – and a potential emission line between 6–7 keV. Expecting the latter to be a broad Fe Kα line, we include a gaussian initially centred at 6.4 keV to the model. The best fit places it at 6.44 ± 0.15 keV and the calculated upper limits for the equivalent widths (EW) for different lines with full widths at half maximum (FWHM) of 0.25, 0.5 and 1.0 keV are 49, 58 and 72 eV, respectively. A simple test is also performed to verify the likelihood of the presence of the 6.4 keV feature in the data. We compare the expected counts from the smooth powerlaw continuum in the region with that of a possible feature superimposed on that continuum and spread along four energy bins centred at 6.08, 6.24, 6.4 and 6.56 keV. The χ^2 statistics can be defined as

$$\chi_4^2 = \frac{\sum_{i=1}^{4}(\text{data}_i - \text{model}_i)^2}{\sigma^2}, \tag{1}$$

where data$_i$ and model$_i$ refer to the four bins closer to the 6.4 keV feature and σ, the same for all four bins, is estimated from the four energy bins just before and after the expected 6.4 keV line. The χ_4^2 for the real data gives a value of 41.54, as opposed to a median χ_4^2 of 3.35 for 10^6 randomly generated sets of four bins. This suggests that a line feature is required to better describe the spectrum in this region with a confidence of 1 : 10^8 parts (roughly 5.7 σ in a normal distribution).

Table 1. Summary of the observations with the date, exposure time and the individual best-fitting powerlaw indices.

Telescope	Observation Date	Exposure Time (s)	Γ
XMM - PN	02/10/2005	16,040	1.77 ± 0.04
NuSTAR - FPMA	03/07/2012	10,970	1.76 ± 0.03
INTEGRAL - ISGRI	13/08/2012	9,332	1.79 ± 0.10

2.2 *XMM* and *INTEGRAL*

Based on the individual powerlaw index that best fitted the *NuSTAR* observation, we chose two observations – from PN, on-board *XMM-Newton* (ObsID 0303210201) and from IS-GRI, on-board *INTEGRAL* (Revolution 1200) – to build a broadband spectrum. Data from these instruments were reduced using each mission's standard procedures: The *XMM-Newton* Science Analysis System (SAS) for PN and *INTEGRAL* Off-line Scientific Analysis (OSA) for ISGRI. A summary of the observations (including *NuSTAR*) with the date, exposure time and the individual best-fitting powerlaw indices is shown in Table 1. It can be noticed that the observations were not contemporary; *XMM* and *NuSTAR* observations are separated by almost 7 years. The primary argument for a simultaneous fit is the very similar photon indices (last column of Table 1), suggesting that 1E 1740.7−2942 was in the same spectral state on the three occasions.

Additional support for combining the spectra comes from the long–term light curve provided by the Burst Alert Telescope (BAT) on-board the *Swift* satellite (Gehrels et al. 2004) which allows us to examine and compare the flux of 1E 1740.7−2942 during the epochs it was observed by *XMM* and *NuSTAR*. The BAT instrument has been monitoring the sky since ∼ 2005 and provides daily count rates for many astrophysical sources in the 15–50 keV band. The upper panel of Figure 2 displays the daily flux for 1E 1740.7−2942 from 2005 February 14 (MJD 53415) to 2013 April 1 (MJD 56383). The observation dates of *XMM* (MJD 53645) and *NuSTAR* (MJD 56111) are indicated by the blue and magenta solid lines, respectively; the dotted boxes with the same colours delimit 50 days before and after these dates, which are displayed in detail in the lower panel. During the whole period, the median flux of 1E 1740.7−2942 in the 15–50 keV band was 8.9×10^{-3} counts·cm^{-2}·s^{-1} with a standard deviation of 5.4×10^{-3} counts·cm^{-2}·s^{-1}, whilst the flux for *XMM* and *NuSTAR* observation were $7.7 \pm 1.0 \times 10^{-3}$ and $9.0 \pm 0.8 \times 10^{-3}$ counts·cm^{-2}·s^{-1}, respectively. These values express that, despite the long gap between the observations, their fluxes are not only consistent with the total median flux (well within 1σ) but are also marginally comparable to each other considering 1σ error bars in each dataset.

The bluish green dotted lines in the lower panel of Figure 2 point out two near *INTEGRAL* ISGRI observations in time to the *XMM* (Revolution 0361) and to the *NuS-TAR* (Revolution 1200) observations. As a supplementary way to verify the source's behaviour during both periods, we present in Figure 3 a colour-colour diagram for these IS-GRI observations. The diagram is built, for each observation, by extracting light curves for three different energy bands – namely a soft (defined here as 20 to 40 keV), a medium (40 to 60 keV) and a hard band (65 to 80 keV) – and plotting the ratio *hardmedium* bands against the ratio *mediumsoft* bands. In Figure 3, the open symbols represent the colours of IS-
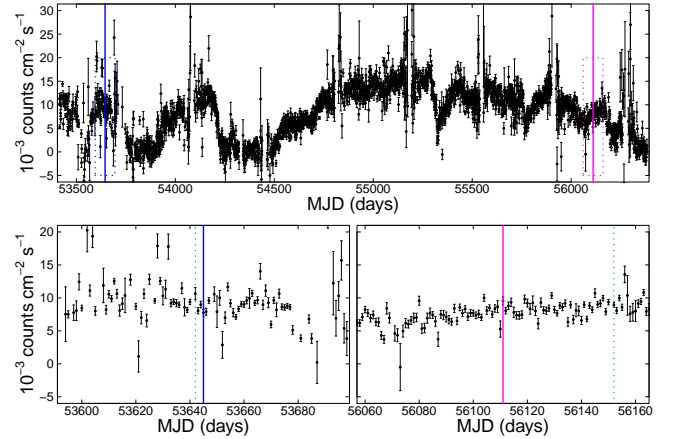
Figure 2. *Upper panel*: Swift BAT long–term light curve for 1E 1740.7−2942. The blue and magenta lines show XMM-Newton and NuSTAR observation dates respectively. *Lower panel*: A zoom of the region delimited by the dotted boxes drawn in the full curve (±50 days from the observations dates). The bluish green dotted lines show the closest INTEGRAL observations.
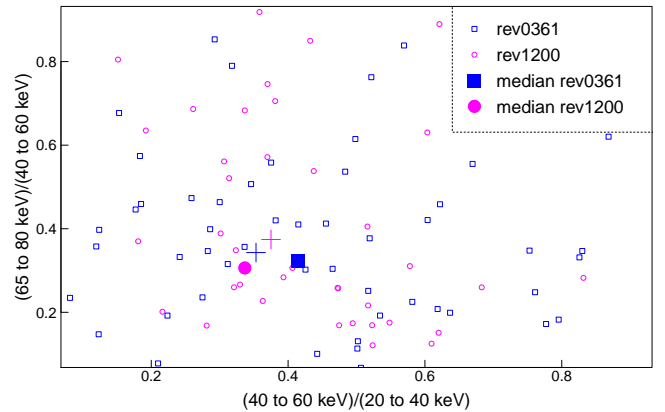

Figure 3. Colour-colour diagram (unfilled shapes) for the IN-TEGRAL observations whose dates were shown in Figure 2. The medians of all the colour ratios for each observation are shown as the slightly bigger filled shapes. The flux ratios for the same bands are also shown (as the plus symbols).

GRI observations closest to *XMM* (squares) and *NuSTAR* (circles) and the slightly larger filled symbols are their corresponding median values. Also shown (as plus symbols) are the flux ratios – for the same energy bands mentioned – calculated for each ISGRI spectra after a powerlaw fit. Their proximity in the diagram indicates that the source was indeed in a very similar state in both occasions. Due to the overlapping energy band, we choose to use the ISGRI observation closer to that of *NuSTAR* (Revolution 1200) to compose the higher energy end of the spectrum.

3 BROADBAND ANALYSIS AND RESULTS

Figure 4 shows the combined spectrum taking into account the considerations from the previous section. The following energy bounds are set for each instrument: *XMM-Newton*:

2–10 keV; *NuSTAR*: 4–60 keV and *INTEGRAL*: 20–200 keV. All models to be described include a multiplicative `constant` to correct the flux offset and all quoted errors are at 90% confidence unless indicated otherwise.

3.1   Powerlaw Models

We initiate the composed spectrum analysis with simpler models and gradually add more complex components. As done for the *NuSTAR* data alone, we start by applying a simple absorbed powerlaw model, which gives a relatively poor fit ($\chi^2\nu = \frac{986}{888} = 1.11$) with large residuals present mainly at lower energies. Values for the interstellar absorption and for the powerlaw index remained within the same range, i.e., N_H ($\times 10^{22}$) $= 12.8 \pm 0.1\,\mathrm{cm}^{-2}$ and $\Gamma = 1.75 \pm 0.01$. Cutoff powerlaw models such as `cutoffpl` or the combination `highecut*powerlaw` provide similar results and set lower limits for the cutoff energy of $\sim 230\,\mathrm{keV}$ and $\sim 216\,\mathrm{keV}$, respectively. A broken powerlaw (`bknpo`) improves the fit ($\chi^2\nu = \frac{939}{886} = 1.06$) and gives indices of $\Gamma = 1.51 \pm 0.10$ and 1.75 ± 0.02 with a break energy of $5.4 \pm 0.5\,\mathrm{keV}$, suggesting the need of another component at lower energies.

A significant fit improvement ($\chi^2\nu = \frac{923}{886} = 1.04$) is then achieved when a multicolour blackbody disc is included in the model (F-test probability of $\sim 10^{-13}$). The `diskbb` model has only two parameters: the inner disc temperature energy and a normalisation factor. The former is found to be $0.19 \pm 0.05\,\mathrm{keV}$ for our fit, value in agreement with previously reported values (see, e.g., Castro et al. 2014). From the latter parameter – the normalisation factor – the inner disc radius may be estimated, as its value is defined by *norm* $\sim (\mathrm{R_{in}}/\mathrm{D_{10\,kpc}})^2 \cos\theta$. Adopting the distance to the Galactic Centre – 8.5 kpc – as the distance to 1E 1740.7−2942 and an inclination of 60°, the lower and upper limits for the normalisation reveal inner radii varying roughly from 25 R_g to 40 R_g for a $10\,\mathrm{M_\odot}$ mass black hole. These limits are in agreement with the radii values reported by Reynolds & Miller (2010) and Natalucci et al. (2014) and support the growing body of evidence contradicting the standard idea in which the disc is truncated at *very* large radii for sources in the LHS. From this model we have also calculated an unabsorbed flux (2–200 keV) of $\approx 3.2 \times 10^{-9}\,\mathrm{erg \cdot cm^{-2} \cdot s^{-1}}$ which – for the same distance and mass previously assumed – corresponds to $\sim 2\%$ of the Eddington luminosity.

3.2   Comptonisation Models

Maintaining the `diskbb` component we tried a few comptonisation models [1] for the hard part of the spectrum. We start with `comptt` (Titarchuk 1994), a model describing comptonisation of blackbody-like seed photons in a hot plasma. Unlike reported by Bouchet et al. (2009) and Castro et al. (2014), this model provides a very high plasma temperature $kT_e > 276\,\mathrm{keV}$ and a very low optical depth τ of 0.08 ± 0.02. Although these values are consistent with the $\tau - kT_e$ degeneracy characteristic for a thermal comptonisation spectrum (see, e.g., Petrucci 2008), they are not typical for black holes

---

[1] For all models with the seed photons temperature as a parameter, we have assigned it to that of the disc temperature from `diskbb`, i.e., $kT_\mathrm{seed} = kT_\mathrm{diskbb}$.
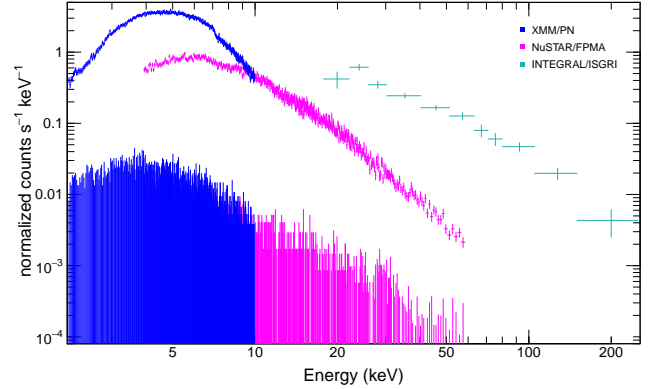

Figure 4. Composed spectrum and background of 1E 1740.7−2942 with XMM/PN (blue), NuSTAR/FPMA (magenta) and INTEGRAL/ISGRI (bluish green) spectra.

in the LHS. None the less – and in detriment of fit quality ($\chi^2\nu = \frac{924}{885} = 1.04$ against $\chi^2\nu = \frac{949}{886} = 1.07$) – by freezing parameter τ at 1 we can retrieve the expected plasma temperature of $\sim 50\,\mathrm{keV}$ (i.e., as reported by studies previously mentioned). The `nthcomp` model (Zdziarski et al. 1996) provides no noticeable difference in the fit quality ($\chi^2\nu = \frac{923}{885} = 1.04$) and the electron temperature also pegs at the model hard limit, however with a lower limit value ($kT_e > 115\,\mathrm{keV}$).

We also apply `compps` (Poutanen & Svensson 1996), which computes comptonisation spectra for different geometries and takes into account reflection from the cold disc. By assuming a spherical and Maxwellian electron distribution for the corona (i.e., only thermal emission), a non-ionised disc ($\xi = 0$), a relative iron and metal abundances varying only between 1 and 3 (based on previous reports by Sakano et al. 1999 and Reynolds & Miller 2010) and a viewing angle of 60°, the model sets constraints on the plasma temperature: $222\,\mathrm{keV} \leq kT_e \leq 426\,\mathrm{keV}$ with an optical depth of $0.19 \leq \tau \leq 0.48$. A reflection component up to $\Omega 2\pi \sim 0.38$ is also detected and will be discussed in the following subsection. This latter model provides the best fit so far ($\chi^2\nu = \frac{911}{882} = 1.03$) – which is further improved ($\chi^2\nu = \frac{901}{882} = 1.02$) if a partially ionised disc ($\xi = 1000\,\mathrm{erg \cdot cm \cdot s^{-1}}$) is considered, yielding values closer to those expected for the source state: $48\,\mathrm{keV} \leq kT_e \leq 282\,\mathrm{keV}$ and $0.67 \leq \tau \leq 2.89$ (also an amount of reflection $\Omega 2\pi \lesssim 0.19$).

Additionally, we apply the `bmc` model (Titarchuk et al. 1997), which considers a more general case where the comptonisation spectrum may be either from a hot corona or from bulk-motion upscattering. Since this model is described as a self-consistent convolution (rather than an additive combination) of powerlaw and seed photons spectrum, the `diskbb` component may be removed. The output parameters for the `bmc` fit ($\chi^2\nu = \frac{923}{886} = 1.04$) are consistent with those found for the `diskbb+powerlaw` model, i.e., $kT_\mathrm{seed} \approx 0.17\,\mathrm{keV}$ and $\alpha \approx 0.76$, where $\alpha = \Gamma - 1$. The model has another parameter, A, that is related to the ratio of photons upscattered via bulk-motion to the photons thermally comptonised in the corona (see, e.g., Borozdin et al. 1999). The limits provided for this parameter indicate practically none ($< 0.5\%$) to 20% dynamically upscattered photons, i.e., this mechanism is not the dominant for our spectrum.

Table 2. Spectral Fit Parameters

Model/Parameter	N_H ($\times 10^{22}\,cm^{-2}$)	Γ	T_{in} (keV)	Γ_2	$E_{fold/break}$ (keV)	kT_e (keV)	τ	$\log_A$	ξ (erg·cm·s^{-1})	Reflection ($\Omega 2\pi$)	$\chi^2/\nu\chi_r^2$
powerlaw	12.8±0.1	1.75±0.01	-	-	-	-	-	-	-	-	986/888/1.11
cutoffpl	12.7±0.1	1.72±0.02	-	-	>233	-	-	-	-	-	978/887/1.10
highecut*powerlaw	12.7±0.1	1.71±0.02	-	-	>215	-	-	-	-	-	973/886/1.10
bknpo	11.9±0.3	1.51±0.01	-	1.75±0.02	$5.43^{+0.71}_{-0.20}$	-	-	-	-	-	939/886/1.06
diskbb+powerlaw	13.3±0.2	1.77±0.01	0.19±0.05	-	-	-	-	-	-	-	923/886/1.04
diskbb+comptt	13.2±0.2	-	0.18±0.05	-	-	>276	<0.1	-	-	-	924/885/1.04
diskbb+comptt	12.8±0.1	-	0.15±0.05	-	-	46.7±1.2	1*	-	-	-	949/886/1.07
diskbb+nthcomp	13.3±0.2	1.77±0.01	0.19±0.05	-	-	>114	-	-	-	-	923/885/1.04
diskbb+compps	12.4±0.2	-	0.15±0.05	-	-	325^{+146}_{-63}	$0.30^{+0.22}_{-0.13}$	-	0*	$0.27^{+0.21}_{-0.06}$	911/882/1.03
diskbb+compps	13.2±0.2	-	0.17±0.05	-	-	82^{+200}_{-34}	$1.69^{+1.2}_{-0.9}$	-	1000*	$0.13^{+0.05}_{-0.03}$	901/882/1.02
bmc	13.3±0.2	^{a}1.77±0.01	0.17±0.05	-	-	-	-	$-1.47^{+0.80}_{-1.00}$	-	-	923/886/1.04
diskbb+pexrav	13.2±0.3	1.75±0.03	0.19±0.05	-	-	-	-	-	^{b}_	$0.12^{+0.08}_{-0.06}$	920/882/1.04
diskbb+pexriv	13.1±0.2	1.75±0.02	0.18±0.05	-	-	-	-	-	1000*	$0.16^{+0.06}_{-0.03}$	904/882/1.02
diskbb+pexriv	12.9±0.2	1.74±0.02	0.16±0.05	-	-	-	-	-	5000^{+0}_{-3592}	$0.12^{+0.09}_{-0.03}$	899/881/1.02
diskbb+powerlaw+reflionx	13.0±0.2	1.71±0.05	0.16±0.05	-	-	-	-	-	6480^{+0}_{-3703}	-	904/883/1.02
diskbb+xillver	12.9±0.1	1.70±0.02	0.16±0.05	-	-	-	-	-	$^c4897^{+2515}_{-1878}$	$0.25^{+0.14}_{-0.06}$	904/882/1.02
diskbb+xillver+comptt	13.0±0.2	-	0.16±0.05	$^d1.85^{+0.22}_{-0.14}$	-	327^{+163}_{-54}	$0.10^{+1.58}_{-0.01}$	-	$^e5248^{+2880}_{-2493}$	-1*	900/881/1.02

Notes: Errors are at 90% confidence limit determined via the error command in XSPEC. All models include a multiplicative constant and the interstellar absorption model phabs. For models in which the relative iron/metal abundances are free parameters, we set them to vary between 1–3, as well as the system's inclination was fixed at 60° (see text for details). An asterisk (*) next to a parameter means that it was frozen at that value. Errors +0 indicate that the parameter reached the allowed hard limit for the model.
^{a}The spectral index of bmc is actually parametrised by α ($=0.77$) and $\Gamma = \alpha + 1$.
^{b}pexrav describes reflection from neutral material, i.e., equivalent to pexriv for $\xi = 0$.
^{c,e}The output ionisation parameter is provided by xillver as $\log \xi$; the original output values were $3.69^{+0.18}_{-0.21}$ and $3.72^{+0.19}_{-0.28}$, respectively.
^{d}As for this combination the xillver model is set to return only the reflected component, this Γ refers to the reflected photon index.

3.3 Non-Relativistic Reflection Models

The fact that the best fit from the comptonisation models occurs for compps – a model that includes a reflection component – suggests that this component may be present in the data and needs to be taken into account. Model compps follows the computational method of the widely used angle-dependent non-relavistic reflection models pexrav and pexriv (Magdziarz & Zdziarski 1995). By applying these two models, for the same initial conditions we set for compps, we find reflection fraction values around 20% for either neutral (pexrav) or partially ionised (pexriv, $\xi = 1000\,erg·cm·s^{-1}$) discs. As it happened for compps, the scenario with a partially ionised disc provides a better fit ($\chi^2\nu = \frac{904}{882} = 1.02$ against $\chi^2\nu = \frac{920}{882} = 1.04$). If ionisation parameter is let free, best fit from pexriv sets it to its hard limit, $5000\,erg·cm·s^{-1}$.

When applying the constant density ionised disc model reflionx (Ross & Fabian 2005) – which does not provide a reflection fraction – an ionisation of $\approx 6500\,erg·cm·s^{-1}$ is obtained. As reflionx is a pure reflection model, a powerlaw was included to represent the continuum and their photon indices tied. The reflection code xillver (García et al. 2013) yields a reflection fraction $R \approx 0.25$ and an ionisation parameter of ≈ 4900 ($\log \xi = 3.69$). This latter uses the coronal geometry and considers the incident spectrum to be a cutoff powerlaw. A different flavor of the model, xillvercp, allows for a nthcomp incident spectrum; however, the soft seed photons energy is not a free parameter and is set to be $kT_{seed} = 0.05\,keV$. Thus, instead, we add the comptt model to describe the incident comptonisation continuum and set xillver to return only the reflected component (by fixing the reflection fraction to −1). In this case, we tie the energy cutoff of the reflected spectrum to twice the kT temperature from comptt. The output comptonisation values for this combination are consistent with those found for the comptt alone and the fit quality slightly improved (F-test probability of $\sim 10^{-5}$). The results for the models applied up to now are presented in Table 2.

3.4 Relativistic Reflection Models

To explore the parameter space for spin and inclination we test a number of relativistic reflection models, which are the essence of the X-ray reflection spectroscopy method *per se*. We start with our previously mentioned fit of reflionx, now convolved with relconv (Dauser et al. 2010) to allow for relativistic effects (diskbb+powerlaw+relconv(reflionx) in XSPEC notation). As before, the photon index of reflionx is tied to that of the powerlaw model. For relconv, we fix the disc outer radius at $R_{out} = 400\,R_g$ and assume the coronal emissivity profile $\epsilon = r^{-q}$ to be unbroken with an emissivity index $q = 3$ (i.e., $q_{in} = q_{out} = 3$). The disc inner radius is initially let frozen at -1, meaning it extends all the way to the R_{ISCO} (radius of the innermost stable circular orbit). The spin and inclination are let free to vary from their model initial default values, i.e., 0.998 and 30°, respectively. Although the best fit ($\chi^2\nu = \frac{897}{881} = 1.02$) for this configuration leaves the spin parameter at its maximum value, $a_* = 0.998$, the parameter reaches both its hard limits (-0.998 and 0.998) when we attempt to calculate the 90% confidence limits. The inclination, however, rapidly increases and is well defined at $63.7^{+4.6}_{-7.9}$ degrees. To investigate how these two parameters behave for different inner radii, we perform further fits for the disc radius fixed at distances (in R_{ISCO} units) of 10, 20,

50 and also free to vary. As the radius increases, the quality of the fit is marginally worsened ($\chi^2 = 899$, 903 and 909, respectively) and the inclination becomes higher and somewhat looser ($75.2^{+10.6}_{-18.9}$, $77.0^{+10.4}_{-22.9}$ and $79.1^{+9.5}_{-52.3}$ degrees). The parameter spin remained at $a_* \simeq 0.998$ for all three scenarios but failed again in providing 90% level limits. For the case where $R_{\rm in}$ is free, the best fit ($\chi^2\nu = \frac{896}{880} = 1.02$) sets the inner radius to ~ 2.5 ($\lesssim 6\,{\rm R_{ISCO}}$ at 90% confidence) and provides an inclination of $61.2^{+3.9}_{-4.9}$ (°); the spin reaches its maximum value but is again not well constrained. Figure 5 shows the $\Delta\chi^2$ variation for these three parameters, calculated via the `steppar` command from XSPEC. Confidence levels at 68.3% ($1\,\sigma$; black dashed line), 90.0% ($1.6\,\sigma$; magenta dashed line), 95.5% ($2\,\sigma$; blue dashed line) and 99.7% ($3\,\sigma$; bluish green dashed line) are indicated. According to the plots, an inner radius truncated at over $\sim 15\,{\rm R_{ISCO}}$ (upper panel) and a disc inclination below $\sim 45°$ or above $\sim 70°$ (middle panel) may be ruled out at $3\,\sigma$ confidence level for this model. The spin parameter (bottom panel) clearly favours the hard limit (> 0.5 at $1\,\sigma$) but still admits any value within $3\,\sigma$. To test whether the disc and the observer see different continua – as pointed out, e.g., by Fürst et al. (2015) and Parker et al. (2016) for GX 339–4 – we repeat the last fit (with $R_{\rm in}$ free to vary) leaving the photon indices of the `powerlaw` and `reflionx` models untied. The powerlaw as seen from the reflector in fact assumes a slightly different index but is also more relaxed and yet in the same range ($\Gamma \sim 2$; $1.5 \lesssim \Gamma \lesssim 2.5$). Contrary to reported in the mentioned studies of GX 339–4 (where a good fit is only achieved for different powerlaw indices), this additional free parameter does not improve our fit ($\chi^2\nu = \frac{896}{879} = 1.02$) nor causes significant changes in the quoted results.

To proceed with the spin and inclination analysis we apply two different coronal geometries available from the `relxill` model family (Dauser et al. 2014; García et al. 2014), i.e., the standard coronal geometry (`relxill` model itself) and the lamp post geometry (`relxilllp`). For the following results, the associated errors are calculated by a Markov Chain Monte Carlo (MCMC) algorithm from Foreman-Mackey et al. (2013), implemented for XSPEC by Jeremy Sanders[2]. As previously done for the non-relavistic version `xillver`, we use `comptt` to describe the primary continuum. For consistency with `relconv(reflionx)`, which also assumes the standard geometry, we adopt the same conditions for `relxill` ($q_{\rm in} = q_{\rm out} = 3$ and $R_{\rm out} = 400\,{\rm R}_g$). For `relxilllp`, that assumes the corona to be a point source at a certain height h above the black hole, we leave this parameter free from its default value ($6\,{\rm R}_g$). We again perform fits for inner radii (in $\rm R_{ISCO}$ units) at 1, 10, 20, 50 and free. The overall outcome with increasing radius, for both combinations, is somewhat similar: the quality of the fit decreases, the disc inclination tends to assume higher values and the spin – still not well constrained – approaches the upper limit for all cases. These variations are presented in Table 3 for the two models (Model 1: `diskbb+relxill+comptt`; Model 2: `diskbb+relxilllp+comptt`). For many parameters no considerable changes between Models 1 and 2 occurred: the ionisation assumes a relatively broad range of $2.3 \lesssim \log\xi \lesssim 3.7$ (log erg·cm·s⁻¹) for any radius for both
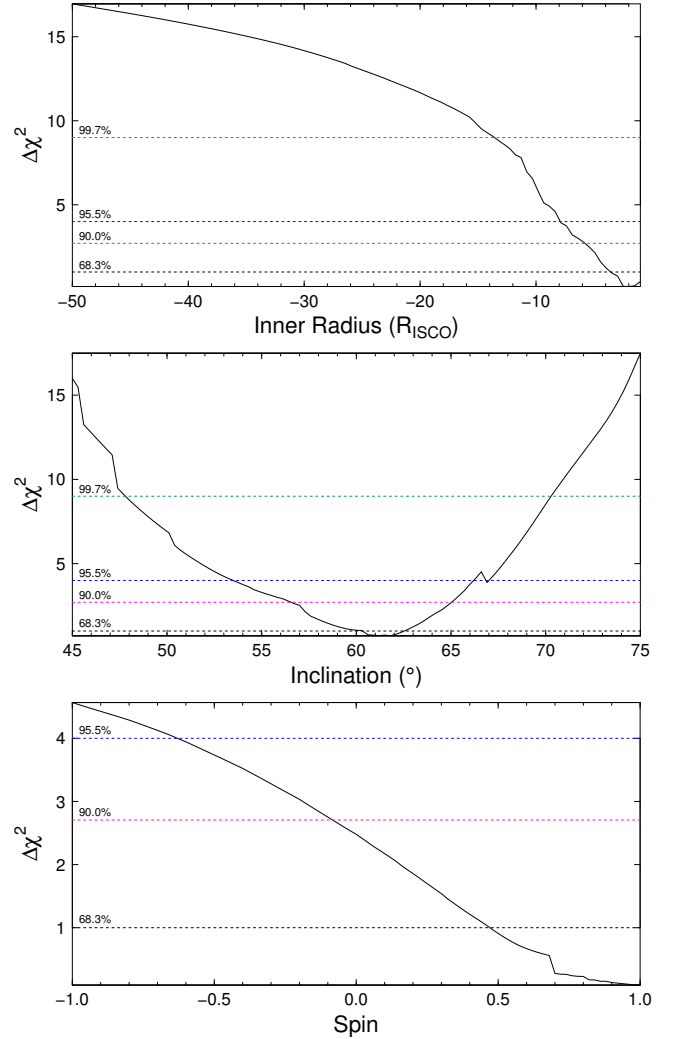
Figure 5. $\Delta\chi^2$ vs parameter value for the inner radius (upper panel), inclination (middle panel) and spin (bottom panel) for the model `diskbb+powerlaw+relconv(reflionx)`. The dashed lines correspond to the confidence levels at 68.3% ($1\,\sigma$; black), 90.0% ($1.6\,\sigma$; magenta), 95.5% ($2\,\sigma$; blue) and 99.7% ($3\,\sigma$; bluish green). **Note:** The negative values in the horizontal axis of the upper panel are merely a model convention and indicate that `relconv` was set to calculate the radius in $\rm R_{ISCO}$ units.

Table 3. Inclination and fit quality for different radii

Model	Parameter	$\rm R_{in}$ ($\rm R_{ISCO}$)			
		1	10	20	50
1	Inclination (°)	$60.8^{+18.3}_{-5.7}$	$72.5^{+11.3}_{-12.8}$	$77.8^{+9.1}_{-25.4}$	$84.9^{+1.5}_{-63.8}$
	$\chi^2\nu$	897/879	899/879	906/879	915/879
2	Inclination (°)	$66.2^{+8.2}_{-10.2}$	$71.3^{+9.4}_{-12.5}$	$72.7^{+6.6}_{-8.6}$	$78.4^{+4.7}_{-9.7}$
	$\chi^2\nu$	899/878	901/878	906/878	907/878

models and the iron abundance raises from the lower to the higher limit we imposed (1 to 3) as the radius increases. For `relxilllp`, the source height varies roughly within the range of $4\,{\rm R}_g \lesssim h \lesssim 13\,{\rm R}_g$ – including errors at 90% confidence level – with the higher values happening for larger radii. The powerlaw indices remain in the same range as that of `reflionx` when left free ($1.5 \lesssim \Gamma \lesssim 2.5$), with no

apparent trend with increasing radius for the coronal geom-
etry and with the powerlaw becoming harder (approaching
the "observer index") for farther inner radii in the lamp-
post geometry. It is interesting to mention that this latter
geometry places the comptonisation parameters in the ex-
pected range for 1E 1740.7−2942, i.e., $30 \, \text{keV} \lesssim kT_e \lesssim 80 \, \text{keV}$
and $0.5 \lesssim \tau \lesssim 2.2$ for any radius. For R_{in} free, the best fit for
Model 1 ($\chi^2\nu = \frac{896}{878} = 1.02$) and Model 2 ($\chi^2\nu = \frac{897}{877} = 1.02$)
yield radii of $2.1^{+4.2}_{-0.3}$ and $5.2^{+4.0}_{-3.1}$ R_{ISCO}, respectively. We
have also performed another fit letting `relxilllp` repre-
sent both incident and reflected spectra alone (Model 3:
`diskbb+relxilllp`), in such a way that we can leave the re-
flection fraction free. The best fit ($\chi^2\nu = \frac{897}{879} = 1.02$), which
sets the inner radius at $1.7^{+9.2}_{-0.6}$ R_{ISCO}, provides a reflection
fraction of $R = 0.26^{+0.27}_{-0.15}$. The powerlaw index – now unique
for both incident and reflected spectrum – is $\Gamma = 1.78^{+0.02}_{-0.05}$.
Other parameters, which are common to Models 1 and 2,
have not changed much from the values quoted previously. In
regard of spin and inclination, Figure 6 presents the MCMC
output distribution for these two parameters for the cases
where R_{in} was left free in Models 1, 2 and 3. For all three
models the spin behaviour differs very little from that of
`relconv(reflionx)`, displayed in the bottom panel of Fig-
ure 5: it reaches the hard limit but is only poorly suggestive
it might be $\gtrsim 0.5$ (1σ); any value is still possible within
3σ. As for the inclinations, they all coincide to be in the
range of ~ 60–$85°$ (2σ); values below $\sim 55°$ can be excluded
with 3σ confidence for Models 1 and 2, whereas for Model 3
this same confidence region encompass a broader range, with
marginally lower inclinations. Model components, model fit-
ted to the data and its residuals for Model 2 are displayed
in Figure 7. Aside from providing the best constraints on
spin and inclination, the reason we elect to show this combi-
nation is that it includes the comptonisation component, in
which best-fitting values of τ and kT_e are – as formerly dis-
cussed – in a more likely interval for 1E 1740.7−2942. For a
comprehensive description of the model variables and depen-
dencies, we also present, in Figure 8, the joint distributions
of selected parameters for Model 2.

3.5 A Putative Mass Estimate Effort

In an attempt to estimate the mass of the black hole,
we replace the component characterising the disc spectrum
for these three last models (with parameter R_{in} free) from
`diskbb` to `kerrbb` (Li et al. 2005). The latter describes a mul-
titemperature blackbody accretion disc around a Kerr black
hole and represents the continuum-fitting method, which
consists of the analysis of the thermal spectrum of a ge-
ometrically thin and optically thick disc in order to mea-
sure the black hole spin (see, e.g., Bambi 2018). Not only
this method relies on an inner disc radius close to ISCO, its
application depends on prior independent measurements of
many parameters – usually inferred from investigations in
other wavelengths – such as the distance to the source, the
inclination of the disc, the accretion rate and the mass of
the black hole. However, as we are interested in the black
hole mass, we follow the approach performed by Parker et
al. (2016) for GX 339–4 and use the inclination and spin
values provided by the reflection model *as input* param-
eters for `kerrbb`. Namely, we tie the spin and inclination
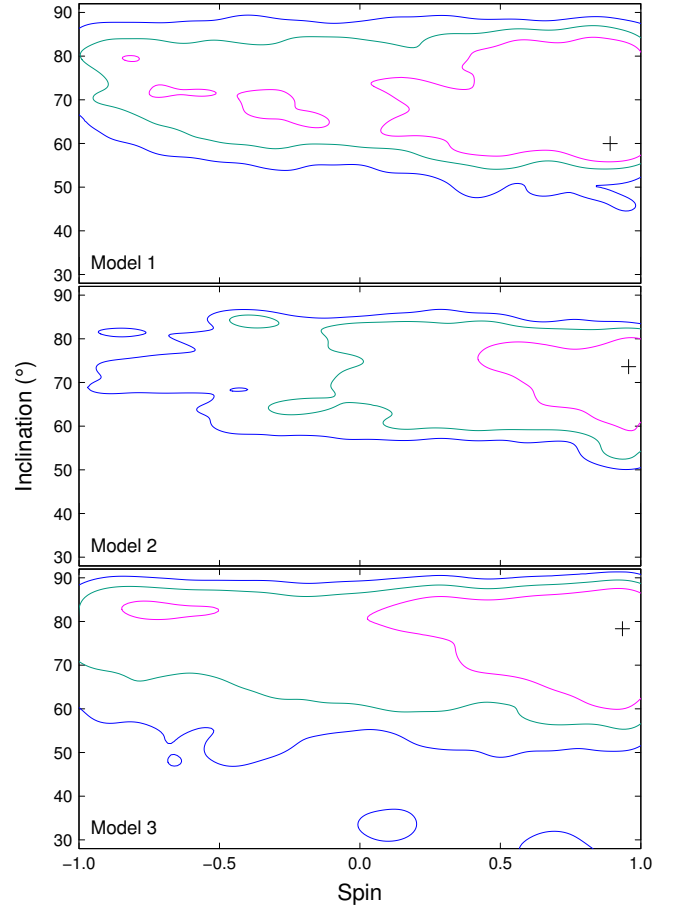

Figure 6. MCMC output distribution for parameters spin and
inclination for combinations `relxill+comptt` (Model 1; upper
panel), `relxilllp+comptt` (Model 2; middle panel) and `relxil-
llp` alone (Model 3; bottom panel). The black plus symbols indi-
cate the best-fitting values. Confidence contours of 1 (magenta),
2 (bluish green) and 3 (blue) σ are shown.

of `kerrbb` to those from the `relxill` models. Apropos of
other parameters, we set the distance to the source to be
fixed at $8.5 \, \text{kpc}$ and the mass accretion rate is left free to
vary from an initial value of $10^{17} \, \text{g} \cdot \text{s}^{-1}$, which is roughly
$\sim 2\%$ of the Eddington accretion rate for a $10 \, \text{M}_\odot$ black
hole with efficiency $\eta = 0.1$. Another noteworthy parame-
ter is the spectral hardening or colour correction factor f,
whose default value – $f = 1.7$ – is usually a good approxi-
mation for sources with luminosities of few times $0.1 \, \text{L}_{\text{Edd}}$
(Shimura & Takahara 1995). Since for our calculated lumi-
nosity of $\sim 0.02 \, \text{L}_{\text{Edd}}$ this factor most likely assumes lower
values (see, e.g, Table 1 from Davis et al. 2005), we perform
fits with f fixed at 1.3, 1.5 and 1.7. For the model remain-
ing parameters, we adhere to the default scenarios: a disc
with zero torque at the inner boundary ($eta = 0$), effects of
self-irradiation are considered ($rflag = 1$) and the disc emis-
sion is assumed to be isotropic ($lflag = 0$). Figure 9 shows
the resulting black hole mass for the three model combina-
tions (Model 1*: `kerrbb+relxill+comptt`; Model 2*: `ker-
rbb+relxilllp+comptt`; Model 3*: `kerrbb+relxilllp`) for
the respective factors f. The masses indicated are the me-
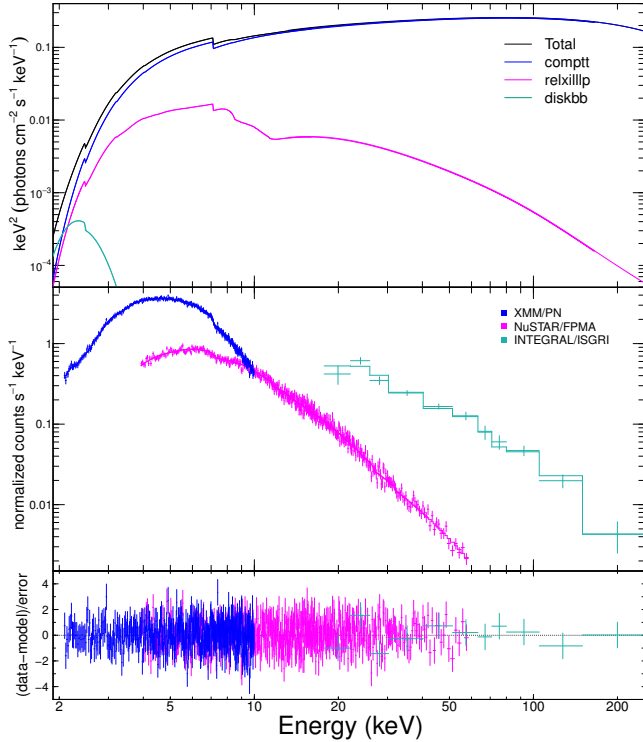dian values of the probability density distribution provided

Figure 7. Model components (upper panel), model fitted to the data (middle panel) and its residuals (bottom panel) for Model 2. **Note:** Vertical axis of bottom panel is in *(data-model)/error*, equivalent to $\Delta\chi$, so magnitudes of *XMM* (blue), *NuSTAR* (magenta) and *INTEGRAL* (bluish green) residuals are comparable.

by an MCMC run from the best-fitting parameters; 68% and 90% confidence level bars shown were calculated from this value. From Figure 9 we can assert that, conservatively, the resulting black hole masses lie within 3 to $10\,M_\odot$; Model 2* provides again the best constraints: $3.9\,M_\odot \lesssim M_{BH} \lesssim 6.1\,M_\odot$ at 90% confidence. It can also be noticed that, apart from slight differences in the mass values for Model 1*, no prominent variation occurs for the mass with respect to the spectral hardening. This also extends to the quality of the fit and to the other parameters, both between the same model for different factors and between the models before and after the disc component was replaced. In other words, most (if not all) parameters were insensitive to the spectral hardening and `kerrbb` model could fit the lower energy part of the spectrum just as well as `diskbb`. As to the mass accretion rates, values varied roughly from 0.002–0.04 ($\times 10^{17}\,g \cdot s^{-1}$), regardless of the model or spectral hardening.

3.5.1 Fits with the `simpl` comptonisation model

It has been pointed out in Steiner et al. (2009b) that when applying the continuum-fitting method, the use of additive combinations – such as a disc plus a powerlaw or plus a comptonisation model – might be inadequate, as these additive models fail to correctly account for the soft component's contribution to the powerlaw spectrum. Instead, the `simpl` model (Steiner et al. 2009a), which self-consistently generates the compton component from the thermal seed photons, should be applied. Therefore, we did the fits of

Table 4. Best-fit parameters with the `simpl` model combinations

Parameter	Model 0S*	Model 1S*	Model 2S*
N_H ($\times 10^{22}\,cm^{-2}$)	$13.4^{+0.1}_{-0.3}$	$13.3^{+0.2}_{-0.3}$	$13.3^{+0.1}_{-0.2}$
Γ	$1.78^{+0.2}_{-0.3}$	$1.79^{+0.3}_{-0.5}$	$1.77^{+0.3}_{-0.8}$
f_{SC}	0.04 ± 0.01	0.03 ± 0.01	0.03 ± 0.01
R_{in} (R_{ISCO})	$2.3^{+6.2}_{-1.2}$	$1.8^{+4.2}_{-0.7}$	$2.45^{+7.5}_{-1.0}$
Inclination (°)	$70.4^{+9.1}_{-9.2}$	$74.3^{+8.5}_{-12.0}$	$73.1^{+7.5}_{-12.9}$
Spin	$0.90^{+0.07}_{-1.31}$	$0.87^{+0.11}_{-1.25}$	$0.87^{+0.12}_{-1.55}$
$\log\xi$	$2.41^{+0.15}_{-0.19}$	$2.47^{+0.98}_{-1.49}$	$2.74^{+0.85}_{-0.69}$
Fe/Solar*	1.14	1.9	2.6
Corona height (R_g)	-	-	$9.7^{+8.5}_{-4.0}$
$\chi^2\nu\chi^2_r$	900/879/1.02	897/879/1.02	898/878/1.02

Notes: Errors are at 90% confidence limit. *This parameter was left free but limited to assume values within 1–3.

Model 1* and Model 2* again (now to be called Model 1S* and Model 2S*, respectively) replacing the additive combination `kerrbb+comptt` to the convolution `simpl(kerrbb)`. We also apply `simpl(kerrbb)` to the `relconv(reflionx)` fit, i.e., `simpl(kerrbb)+relconv(reflionx)` – which we name Model 0S*. The `simpl` model is parametrised by only two parameters: the photon index Γ and the scattered fraction f_{SC}; the latter, by default, provides the fraction of photons from the accretion disc that are upscattered in energy by the corona. As before, we perform three fits for each, with the spectral hardening f fixed at 1.3, 1.5 and 1.7. We find, again, that no substantial differences are caused by the choice of this parameter. Likewise, the output parameters for the best-fits were all in the same range as the ones quoted in the previous subsections. The resulting masses for all cases are shown in Figure 10 (displayed in the same way of Figure 9) and some parameters of interest are shown in Table 4, for the intermediate case of $f = 1.5$.

4 DISCUSSION

We have gathered public available X-ray data from *XMM-Newton*, *NuSTAR* and *INTEGRAL* to build a broadband spectrum (2–200 keV) of the black hole candidate 1E 1740.7−2942. Since the observations were not taken contemporaneously, arguments regarding the flux and emission state of the source for each epoch were presented to justify a simultaneous analysis. We present on the application of several models that describe the three main spectral features of this type of source; the disc, reflection and comptonisation components. The composed spectrum is visually featureless and a relatively good fit ($\chi^2\nu \sim 1.04$) could already be achieved with a simple disc + powerlaw combination. We have shown, however, that the upgrade to models that account for a reflection feature improves the quality of the fit ($\chi^2\nu \sim 1.02$); when applicable (i.e., the reflection component was simply added to a combination), F-test values expressed such improvement. As we dealt with many model combinations – most of which are not nested – a more sophisticated way to compare the relative quality of fit for different mod-
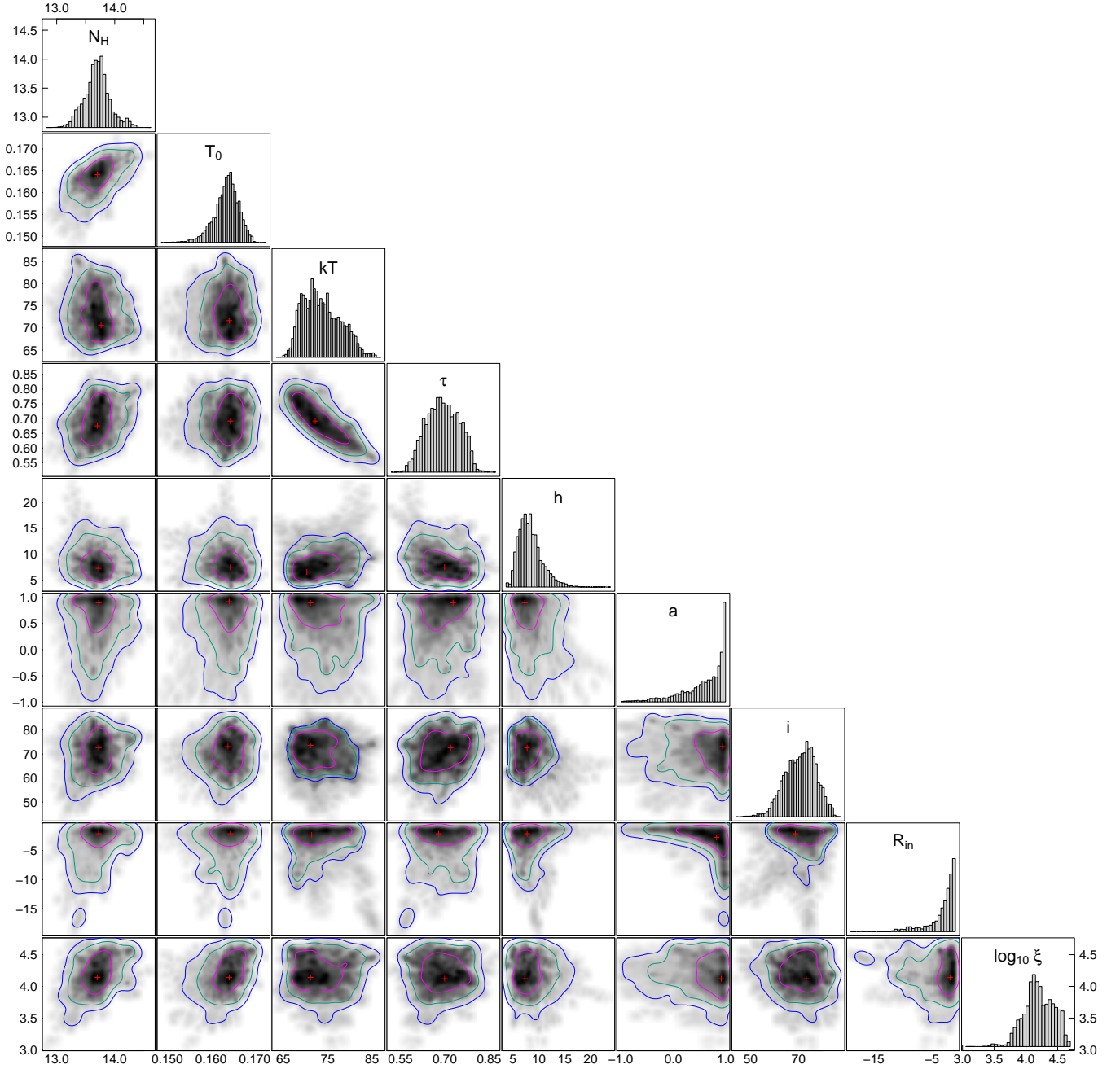
Figure 8. Joint distribution of selected parameters for Model 2, calculated from the MCMC output. The red plus symbols indicate the best-fitting values. Confidence contours of 1 (magenta), 2 (bluish green) and 3 (blue) σ are shown. **Note:** Parameters and their units are: N_H ($\times 10^{22}\,\mathrm{cm}^{-2}$), T_0 (keV), kT_e (keV), h (R_g), i (degrees), R_{in} (R_{ISCO}), $\log\xi$ ($\log\,\mathrm{erg}\cdot\mathrm{cm}\cdot\mathrm{s}^{-1}$). τ and a are dimensionless.

els is using the Akaike Information Criterion (AIC, Akaike 1974). The AIC for each model i is given by

$$\mathrm{AIC}_i = 2m - C + \chi^2 + \frac{2m(m+1)}{n-m-1}, \qquad (2)$$

where m is the number of free parameters, n is the number of energy bins and C is a value that depends only on the data set and thus, is constant for every model. Lower values of AIC indicate better models. Moreover, the probability of a certain model to be the best among a set of models can be computed with the Akaike Weights (Akaike 1978), which

express the probability that a model i is the best among k models. It is defined as

$$p_i = \frac{\exp(-\Delta\mathrm{AIC}_i 2)}{\sum_{i=1}^{k} \exp(-\Delta\mathrm{AIC}_i 2)}, \qquad (3)$$

with $p_k = 1$ and where $\Delta\mathrm{AIC}_i = \mathrm{AIC}_i - \min(\mathrm{AIC})$. When computing this to all model combinations we applied, the ones *without* a reflection component hold a probability of less than 0.5% of being the best-fitting models. This means that although the reduced χ^2 among fits differs only in the second decimal place for models with and without reflection,
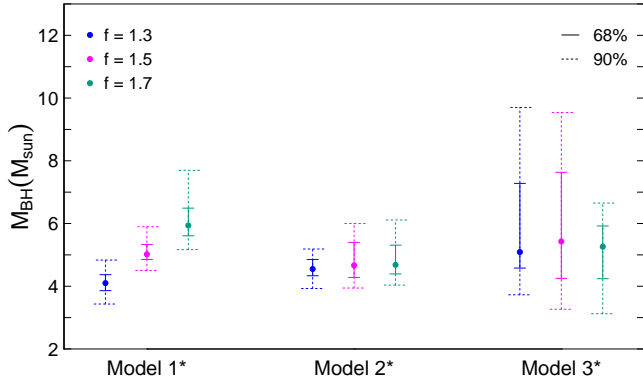
Figure 9. Output mass values for Models 1*, 2* and 3* for spectral hardening factors of $f = 1.3$ (blue), 1.5 (magenta) and 1.7 (bluish green). Solid and dashed bars indicate 68% and 90% confidence respectively (see text for details).
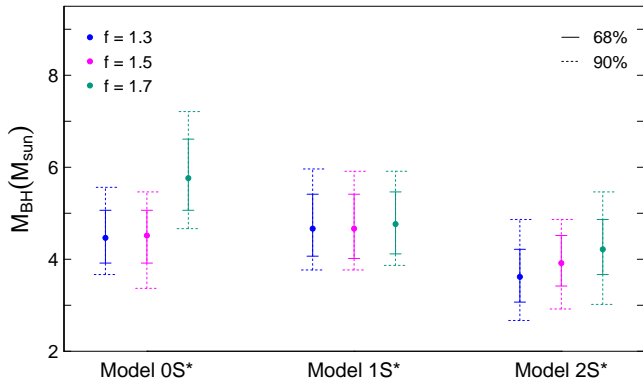

Figure 10. Same as Figure 9, now for Models 0S*, 1S* and 2S* (see text for details).

it is very likely that this component – whether relativistic or not – is required to properly describe the data. In the following subsections we briefly discuss about the overall resulting values presented throughout the text.

4.1   The Emission State

Black hole emission states have been customarily discriminated by the indices of phenomenological powerlaws fitted to their higher energy part of the spectrum; being a steeper index indicative of the high/soft state (HSS) state and a less steep of the LHS. The powerlaw indices found for our spectra – individually or combined – are somewhat steeper than values previously reported for 1E 1740.7−2942. Also different from most reports is the absence of a cutoff energy up to ∼ 200 keV and an atypical higher corona temperature (for some of our models). None the less, with comparable energy coverage from *Suzaku*, Reynolds & Miller (2010) reported very similar indices ($\Gamma \sim 1.8$) and high energy cutoffs to what we found, in epochs they denoted as being right after a transition from the HSS to the LHS. Since there are so far no reports of 1E 1740.7−2942 being observed in the soft state, we believe this classification was most likely based on the fact that their observations occurred after periods of virtually no

detection in the 15–50 keV band from BAT daily flux measurements. As in our study we simultaneously analyse non-contemporaneous data, other than affirming 1E 1740.7−2942 was in a "softer" LHS for the observations, we can not state anything about the source being after or before a transition. Our calculated luminosity (2–200 keV) of less than a few percent of Eddington's also corroborates with a black hole in the LHS.

4.2   Disc Requirement and Truncation

Previous studies with *Suzaku* (Reynolds & Miller 2010) and *NuSTAR* (Natalucci et al. 2014) have reported the need to account for a softer component to fit the spectrum of 1E 1740.7−2942 down to energies of 2 and 3 keV, respectively. In fact, significant fit improvement is achieved when we include a disc component – both when fitting our *NuSTAR* data alone (> 3 keV, F-test probability of ∼ 10^{-6} against no disc) and, even more explicit, when fitting with *XMM-Newton* data included (down to 2 keV, F-test probability of ∼ 10^{-13}). This reveals that, despite the very high interstellar absorption towards the source's location, a multitemperature accretion disc is required to describe 1E 1740.7−2942 spectra above a few keV. Also in agreement with the mentioned studies is our estimation of the disc inner radius, which we find – from the normalisation of the disc component – to be no more than $60\,R_g$. When evaluating this same quantity from modelling the reflection component, our results suggest an even less truncated disc. From performing fits for various reflection models and different inner radii distances from the black hole up to $50\,R_{ISCO}$ (roughly $60\,R_g$ for a Kerr black hole) we notice that the fit quality consistently decreases for increasing radius. When let free, overall best-fits imply the radius is no farther than ∼ $15\,R_{ISCO}$ (∼ $20\,R_g$) from the compact object at $3\,\sigma$ level confidence. Hence, from our results, 1E 1740.7−2942 may be another evidence to support that discs for black holes in the LHS are not necessarily truncated at very large distances (e.g., see Tomsick et al. 2008 for GX 339−4, Parker et al. 2015 for Cyg X−1 and Xu et al. 2018 for MAXI J1535–571).

4.3   The Reflection Component

A hint of a skewed iron line and a compton hump in our *NuSTAR* data prompted us to include models to describe these reflection features which, as previously pointed out, improved the quality of the fit – endorsing its presence in the spectrum. Based on the possibility of the disc inner radius being close to the black hole, we advanced to relativistic reflection models, whose main parameters of interest are the spin of the black hole and the inclination of the disc. All model combinations indicate a high spin and a high inclination. Every best fit sets the parameter spin to values close to that of a maximum speed rotating black hole ($a_* = 0.998$), some with $1\,\sigma$ confidence that $a_* \gtrsim 0.5$. Reports of high spin values for black holes in binary systems are very frequent, particularly when the estimate procedure used is the iron line method (see, e.g., Table 2 from Bambi 2018). None the less, despite this trend, our assessment is that our models could not adequately constrain the spin. As for the disc inclination, best-fitting values vary roughly

from 60° to almost 80° among models but they all agree, within 3σ, that it is $\gtrsim 50°$. These inclinations are consistent with the bi-polar radio jets presence reported by Mirabel et al. (1992). More recently, Luque-Escamilla et al. (2015) obtained constraints on the jets inclination, whose values – if assumed the disc-jet perpendicularity – are also consistent with fairly high inclination for the accretion disc. Such high inclinations would suggest that detectable eclipses should occur. However, in both reports on the orbital period (~12.6 days) of 1E 1740.7−2942 – from long–term time analysis in different X-ray bands (2.5–12.5 keV, Smith et al. 2002; and 15–50 keV, Stecchini et al. 2017) – no obvious shape of an eclipse was identified. This could be due to an extended hard X-ray emitting source that is only partially obscured by the companion star. With an extended corona, either in length or height, photons reprocessed in the disc could be subject to being upscattered in the corona again – a scenario that would be in agreement with the not very pronounced reflection feature in our spectrum and with the small reflection fraction values we find (see, e.g., Wilkins & Gallo 2015).

4.4 The Mass

A virtually identical fit quality can be achieved when the simple multitemperature `diskbb` model – parametrised only by its inner temperature – is replaced by `kerrbb`, a much more complex model dependent on several parameters. Different choices for the spectral hardening value have not caused significant changes in the mass, spin, accretion rate or inclination. This weak relationship between f and these parameters had been demonstrated by Shimura & Takahara (1995) and also, e.g., recently verified (Sridhar et al. 2019). The extremely low accretion rates such as the ones we find (equivalent to roughly $\sim 10^{-11}\,\mathrm{M_\odot \cdot yr^{-1}}$) had been reported for black hole binaries in the "quiescent" state (see, e.g., Pal & Chakrabarti 2004 and references therein). Narayan et al. (1998) argue that for such accretion inefficiencies, the thin disc approximation is no longer valid and that the inner part of the disc would be better described by an advection-dominated accretion flow model; this issue is, however, beyond the scope of this paper. Finally, overall results suggest a relatively low black hole mass in 1E 1740.7−2942, with a median best-fitting value of $4.7\,\mathrm{M_\odot}$ amongst all 18 model combinations; in only 2 combinations a mass up to $10\,\mathrm{M_\odot}$ is allowed at 90% confidence level. An inspection of the BlackCAT (Corral-Santana et al. 2016), a catalogue for stellar-mass black holes in X-ray transients, shows that – at its time of publication – 18 low mass X-ray binaries (LMXBs) had the black hole mass dynamically measured (i.e. from the companion's radial velocity measurement method). Considering their uncertainties, roughly all black hole masses lie somewhere within a $5\,\mathrm{M_\odot} \lesssim \mathrm{M} \lesssim 12\,\mathrm{M_\odot}$ range. Additional research in the literature adds 6 more LMXBs with mass estimates to the list, of which 4 were determined by different methods based on X-ray spectra ($10 \pm 0.1\,\mathrm{M_\odot}$ for 4U 1630−47, Seifina et al. 2014; 4.7–$7.8\,\mathrm{M_\odot}$ for MAXI J1659−152, Molla et al. 2016; 10.31–$14.07\,\mathrm{M_\odot}$ for H 1743−322, Bhattacharjee et al. 2017 and 10.62–$12.33\,\mathrm{M_\odot}$ for IGR J17091−3624, Radhika et al. 2018) – as their optical/infrared counterparts have not yet been confirmed . The reported masses also lie in the same range of those LMXBs from the BlackCAT. The situation for high mass X-ray binaries (HMXBs) is more modest, as

only 3 black holes have their masses measured: Cyg X−1, $14.8 \pm 1\,\mathrm{M_\odot}$; LMC X−1, $10.9 \pm 1.4\,\mathrm{M_\odot}$ (see, e.g., Casares & Jonker 2014) and LMC X−3, $6.98 \pm 0.56\,\mathrm{M_\odot}$ (Orosz et al. 2014). As for neutron stars, no more than a couple of objects have been reported to surpass $2\,\mathrm{M_\odot}$ (e.g., Linares et al. 2018, Cromartie et al. 2019). These numbers indicate an absence of compact objects around the 2–$5\,\mathrm{M_\odot}$ mass range, referred for the first time by Bailyn et al. (1998) as the *mass gap*. Thereby, if the estimate presented here of a black hole mass around 4–$5\,\mathrm{M_\odot}$ (i.e., considering the median value from all best fits) is further confirmed, 1E 1740.7−2942 would be one of the first compact objects to populate this gap. It should be pointed out that – due to their positive correlation – by fixing the accretion rate to higher values (e.g., the initial guess) the black hole mass increases accordingly; yet, no statistically acceptable fit could be achieved in these circumstances.

5 CONCLUSIONS

We have presented and discussed the application of several model combinations in order to fit a broadband X-ray spectrum (2–200 keV, built from *XMM-Newton*, *NuSTAR* and *INTEGRAL* data) of the black hole candidate 1E 1740.7−2942, system in which many dynamical parameters are still unknown. Models were applied in gradual increase order of complexity; significant enhancements in the quality of the fit are accomplished when a thermal disc and, further, a reflection component are included – expressing that such components are needed to describe the spectrum. The main conclusions regarding the results from modelling the spectrum are summarised below.

(i) 1E 1740.7−2942 was in a very similar emission state during all three observations, namely the LHS. Although slightly steeper than previously reported for 1E 1740.7−2942, the powerlaw indices found – either for the individual spectra (Table 1) or for the composed spectrum (Table 2) – are still covered by the accepted index range for black holes in the LHS. The Eddington's luminosity calculated and presented for the composed spectrum is also in agreement with a black hole in this state.

(ii) Estimates of the inner disc radius – whether calculated from the disc normalisation ($\lesssim 60\,\mathrm{R_g}$) or from modelling the reflection component ($\lesssim 20\,\mathrm{R_g}$) – indicate an inner disc not far from the compact object; this is somewhat conflicting with the scenario of very truncated accretion discs, widely regarded to be the case for sources in the LHS.

(iii) Computing the Akaike Weights for every model combination we applied shows that the ones that include a reflection component are 99.5% more likely to be the best-fitting models. Results from modelling this component point to a high disc inclination of at least 50° (3σ), which is in agreement with previous studies in radio. The spin parameter, for every best fit, is set to values close to $a_* = 0.998$; however, it is only constrained to be $a_* \gtrsim 0.5$ at 1σ.

(iv) Modelling the low energy part of the spectrum with the mass-dependent disc model `kerrbb` provided black hole mass values with no more than $10\,\mathrm{M_\odot}$. Actually, in only 2 out of 18 model combinations the resulting mass could be as high as this value; the median best-fitting mass value amongst all combinations is only $4.7\,\mathrm{M_\odot}$. If such low mass is

further confirmed, the black hole in 1E 1740.7−2942 would be amongst one of the first compact objects to populate the so-called 2–5 $M_\odot$ *mass gap*.

REFERENCES

Akaike, H. 1974, IEEE Transactions on Automatic Control, 19, 716

Akaike, H. 1978, Annals of the Institute of Statistical Mathematics, 30, 9

Arnaud, K. A. 1996, Astronomical Data Analysis Software and Systems V, 101, 17

Bailyn, C. D., Jain, R. K., Coppi, P., & Orosz, J. A. 1998, ApJ, 499, 367

Bambi, C. 2018, Annalen der Physik, 530, 1700430

Bhattacharjee, A., Banerjee, I., Banerjee, A., Debnath, D., & Chakrabarti, S. K. 2017, MNRAS, 466, 1372

Borozdin, K., Revnivtsev, M., Trudolyubov, S., Shrader, C., & Titarchuk, L. 1999, ApJ, 517, 367

Bouchet, L., del Santo, M., Jourdain, E., et al. 2009, ApJ, 693, 1871

Casares, J., & Jonker, P. G. 2014, Space Sci. Rev., 183, 223

Castro, M., D'Amico, F., Braga, J., et al. 2014, A&A, 569, A82

Corral-Santana, J. M., Casares, J., Muñoz-Darias, T., et al. 2016, A&A, 587, A61

Cromartie, H. T., Fonseca, E., Ransom, S. M., et al. 2019, Nature Astronomy,

Dauser, T., Wilms, J., Reynolds, C. S., & Brenneman, L. W. 2010, MNRAS, 409, 1534

Dauser, T., García, J., Parker, M. L., Fabian, A. C., & Wilms, J. 2014, MNRAS, 444, L100

Davis, S. W., Blaes, O. M., Hubeny, I., & Turner, N. J. 2005, ApJ, 621, 372

del Santo, M., Bazzano, A., Zdziarski, A. A., et al. 2005, A&A, 433, 613

Foreman-Mackey, D., Hogg, D. W., Lang, D., & Goodman, J. 2013, PASP, 125, 306

Fürst, F., Nowak, M. A., Tomsick, J. A., et al. 2015, ApJ, 808, 122

Gallo, E., & Fender, R. P. 2002, MNRAS, 337, 869

García, J., Dauser, T., Reynolds, C. S., et al. 2013, ApJ, 768, 146

García, J., Dauser, T., Lohfink, A., et al. 2014, ApJ, 782, 76

Gehrels, N., Chincarini, G., Giommi, P., et al. 2004, ApJ, 611, 1005

Harrison, F. A., Craig, W. W., Christensen, F. E., et al. 2013, ApJ, 770, 103

Hertz, P., & Grindlay, J. E. 1984, ApJ, 278, 137

Jansen, F., Lumb, D., Altieri, B., et al. 2001, A&A, 365, L1

Li, L.-X., Zimmerman, E. R., Narayan, R., & McClintock, J. E. 2005, ApJS, 157, 335

Linares, M., Shahbaz, T., & Casares, J. 2018, ApJ, 859, 54

Luque-Escamilla, P. L., Martí, J., & Martínez-Aroza, J. 2015, A&A, 584, A122

Magdziarz, P., & Zdziarski, A. A. 1995, MNRAS, 273, 837

Makishima, K., Maejima, Y., Mitsuda, K., et al. 1986, ApJ, 308, 635

Martí, J., Luque-Escamilla, P. L., Sánchez-Sutil, J. R., et al. 2010, ApJ, 721, L126

Mirabel, I. F., Rodriguez, L. F., Cordier, B., et al. 1992, Nature, 358, 215

Mitsuda, K., Inoue, H., Koyama, K., et al. 1984, PASJ, 36, 741

Molla, A. A., Debnath, D., Chakrabarti, S. K., Mondal, S., & Jana, A. 2016, MNRAS, 460, 3163

Narayan, R., Mahadevan, R., & Quataert, E. 1998, Theory of Black Hole Accretion Disks, 148

Natalucci, L., Tomsick, J. A., Bazzano, A., et al. 2014, ApJ, 780, 63

Orosz, J. A., Steiner, J. F., McClintock, J. E., et al. 2014, ApJ, 794, 154

Pal, S., & Chakrabarti, S. K. 2004, A&A, 421, 13

Parker, M. L., Tomsick, J. A., Miller, J. M., et al. 2015, ApJ, 808, 9

Parker, M. L., Tomsick, J. A., Kennea, J. A., et al. 2016, ApJ, 821, L6

Petrucci, P. O. 2008, Mem. Soc. Astron. Italiana, 79, 118

Poutanen, J., & Svensson, R. 1996, ApJ, 470, 249

Radhika, D., Sreehari, H., Nandi, A., Iyer, N., & S, M. 2018, arXiv:1808.05556

Remillard, R. A., & McClintock, J. E. 2006, ARA&A, 44, 49

Reynolds, M. T., & Miller, J. M. 2010, X-ray Astronomy 2009; Present Status, Multi-Wavelength Approach and Future Perspectives, 1248, 189

Ross, R. R., & Fabian, A. C. 2005, MNRAS, 358, 211

Sakano, M., Imanishi, K., Tsujimoto, M., Koyama, K., & Maeda, Y. 1999, ApJ, 520, 316

Seifina, E., Titarchuk, L., & Shaposhnikov, N. 2014, ApJ, 789, 57

Shimura, T., & Takahara, F. 1995, ApJ, 445, 780

Smith, D. M., Heindl, W. A., & Swank, J. H. 2002, ApJ, 578, L129

Sridhar, N., Bhattacharyya, S., Chandra, S., & Antia, H. M. 2019, MNRAS, 487, 4221

Stecchini, P. E., Castro, M., Jablonski, F., D'Amico, F., & Braga, J. 2017, ApJ, 843, L10

Steiner, J. F., Narayan, R., McClintock, J. E., & Ebisawa, K. 2009, PASP, 121, 1279

Steiner, J. F., McClintock, J. E., Remillard, R. A., Narayan, R., & Gou, L. 2009, ApJ, 701, L83

Sunyaev, R., Churazov, E., Gilfanov, M., et al. 1991, ApJ, 383, L49

Titarchuk, L. 1994, ApJ, 434, 570

Titarchuk, L., Mastichiadis, A., & Kylafis, N. D. 1997, ApJ, 487, 834

Tomsick, J. A., Kalemci, E., Kaaret, P., et al. 2008, ApJ, 680, 593-601

Wilkins, D. R., & Gallo, L. C. 2015, MNRAS, 448, 703

Winkler, C., Courvoisier, T. J.-L., Di Cocco, G., et al. 2003, A&A, 411, L1

Xu, Y., Harrison, F. A., García, J. A., et al. 2018, ApJ, 852, L34

Zdziarski, A. A., Johnson, W. N., & Magdziarz, P. 1996, MNRAS, 283, 193

This paper has been typeset from a TEX/LATEX file prepared by the author.